



Full length article

Tensile creep behavior of HfNbTaTiZr refractory high entropy alloy at elevated temperatures



Che-Jen Liu^{a,b}, Christian Gadelmeier^c, Shao-Lun Lu^{d,e}, Jien-Wei Yeh^{a,f}, Hung-Wei Yen^{d,e,*}, Stéphane Gorsse^{g,*}, Uwe Glatzel^{c,*}, An-Chou Yeh^{a,b,f,*}

^a High Entropy Materials Center, National Tsing Hua University, 101, Sec. 2, Kuang-Fu Road, Hsinchu 30013, Taiwan

^b Ph.D. Program in Prospective Functional Materials Industry, National Tsing Hua University, 101, Sec. 2, Kuang-Fu Road, Hsinchu 30013, Taiwan

^c Metals and Alloys, University of Bayreuth, Prof.-Rüdiger-Bormann-Str. 1, 95447, Bayreuth, Germany

^d Department of Materials Science and Engineering, National Taiwan University, No. 1, Sec. 4, Roosevelt Rd., Taipei 10617, Taiwan

^e Advanced Application Centre for Microscopy & Microanalysis, National Taiwan University, No. 1, Sec. 4, Roosevelt Rd., Taipei 10617, Taiwan

^f Department of Materials Science and Engineering, National Tsing Hua University, 101, Sec. 2, Kuang-Fu Road, Hsinchu 30013 Taiwan

^g Univ. Bordeaux, CNRS, Bordeaux INP, ICMCB, UMR 5026, F-33600 Pessac, France

ARTICLE INFO

Article history:

Received 13 April 2022

Revised 12 July 2022

Accepted 18 July 2022

Available online 18 July 2022

Keywords:

Refractory high entropy alloy

Creep

High-temperature deformation

Diffusion

Thermally activated processes

ABSTRACT

Tensile creep, which is one of the most important deformation modes for high temperature applications, is rarely reported for refractory high entropy alloys (RHEAs). In the present study, the optical floating zone (OFZ) technique was used to fabricate HfNbTaTiZr with grain size larger than 1 mm on average; tensile creep tests under vacuum at 1100–1250°C and stepwise loading of 5–30 MPa were conducted. The stress exponents and creep activation energies were determined to be 2.5–2.8 and $273 \pm 15 \text{ kJ mol}^{-1}$, respectively. The stress exponents determined have suggested solute drag creep behavior, and deformation was governed by $a/2<111>$ type dislocations. To elucidate the effect of alloying constituents on solute drag creep, intrinsic diffusion coefficients of all elements were determined by simulation, and theoretical minimum creep strain rates were compared with those of experimental values. Analysis suggests that creep rate of HfNbTaTiZr appears to be controlled by Ta, which possesses the lowest intrinsic diffusivity and contributes the most to drag dislocations. To our knowledge, this work is the first to report tensile creep deformation mechanism of HfNbTaTiZr, especially up to 1250°C.

© 2022 Acta Materialia Inc. Published by Elsevier Ltd. All rights reserved.

1. Introduction

In the early 2000s, the notion of “high entropy alloys” (HEAs) was conceptualized by Yeh et al. [1] and Cantor et al. [2], and it emerged as a new strategy of alloy design. The composition space of alloys that can be explored is literally unlimited with this approach [3–5]. The microstructures of HEAs can also be customized to meet desired properties, including single phase solid solution HEAs [3,4,6–8] and HEAs with hierarchical microstructures [9–12]. Furthermore, second phases can be introduced in systems, such as Co-Cr-Fe-Ni-Ti [13,14], Al-Co-Cr-Fe-Ni [15–22], and high entropy superalloys [23–25]. To propose a potential solution with temperature capability beyond-superalloys, Senkov et al. [26,27] reported refractory high entropy alloys (RHEAs) that constitute

mainly refractory elements, and have since drawn lots of interests to study their mechanical properties, however, reported literatures were mainly based on studies of compression deformation [28–34]. Among all RHEAs, HfNbTaTiZr has attracted lots of attentions, because it possesses a fully disordered BCC solid solution structure with melting point around 1800°C [29,35]. HfNbTaTiZr exhibits a combination of high strength and ductility at room temperature [29,30], and at cryogenic temperatures [36]. HfNbTaTiZr can also retain its compression strength at elevated temperatures, i.e. 790 MPa at 400°C and 675 MPa at 600°C [30]; it has been reported that $a/2<111>$ screw dislocations movements dominate its compression deformation from room temperature to 800°C [37,38].

Tensile creep is one of the most important demands for high temperature applications. However, to the best of authors' knowledge, there has been no literature reported for RHEAs in this subject to-date. Previous works have analyzed the creep behavior of some other refractory alloys. Lin et al. [39] reported creep of Ta-2.5 wt.% W (grain size $\sim 70 \mu\text{m}$) under 1250–1450°C and a stress

* Corresponding authors.

E-mail addresses: homeryen@ntu.edu.tw (H.-W. Yen), stephane.gorsse@icmcb.cnrs.fr (S. Gorsse), Uwe.Glatzel@uni-bayreuth.de (U. Glatzel), yehac@mx.nthu.edu.tw (A.-C. Yeh).

range of 35 to 210 MPa. It showed a transition from solute drag creep (stress exponent, $n = 3$) to dislocation climb creep ($n > 3$) at high-stress regions. Kellner et al. [40] investigated the creep of Mo-9Si-8B based alloys under vacuum at 1250 °C with stresses from 50 to 250 MPa; the stress exponent was found to be 3.8, indicating dislocation climb controlled creep. And, C103, which is a Nb-based alloy was reported to creep by solute drag mechanism under high temperature and low stress conditions [41]. It appears that refractory alloys exhibit various creep mechanisms under different testing conditions. Despite a lack of thorough understanding regarding the creep deformation behavior of RHEAs so far, experiments of HEAs have been conducted to characterize their creep properties [42–50]. However, majority of these studies were based on 3d-transition metals based HEAs, only Kral et al. [46] reported the compression creep behavior of AlTiVNbZr_{0.25} RHEA (B2 matrix + Zr₅Al₃-precipitates) at 800°C and stresses of 100–560 MPa; its creep mechanism was elucidated to be solute drag creep by analyzing the stress exponent ($n = 3$) and an observation of sluggish subgrains formation. So far, there is no report about tensile creep of RHEAs, since RHEAs is a potential candidate for beyond-superalloys applications, it is important to understand the mechanism of tensile creep deformation of the intrinsic high entropy single phase solid solution. In this work, HfNbTaTiZr has been chosen for tensile creep studies at temperatures up to 1250 °C, because of its stability as a single BCC solid solution phase at elevated temperatures, unlike the other RHEAs that exhibit complex phases [33,34,46,51] or inversion between B2 and BCC phase [32,52].

2. Experimental procedure

The HfNbTaTiZr refractory high entropy alloy was prepared from pure elements Hf, Nb, Ta, Ti, Zr with 99.95 wt.% purity. Ingots were produced by vacuum arc-melting on a copper water-cooled cavity. Before alloying, the arc-melting tank was evacuated to 2 Pa, then filled with argon with 99.99% purity, and evacuated again; this process was repeated three times in order to purge the residual atmosphere, and a pure argon atmosphere filled to 34.5 kPa was achieved. Pure Ti ingot was then re-melted inside the chamber to act as getter of residual oxygen and nitrogen. During the alloying and melting process, each ingot was flipped and melted five times to improve the chemical homogeneity, and ingots with dimensions of 15 × 35 × 120 mm³ were produced. Cylindrical rods with 12 mm in diameter and 100 mm in length were obtained from ingots by electrical discharge machining (EDM). Surfaces of the cylindrical rods were then grinded by SiC sandpapers to 800 grit and ultrasonic cleaned in alcohol to ensure no oxide layer remained. The cylindrical samples of HfNbTaTiZr were

Table 1

Testing temperatures and corresponding stresses of tensile creep tests.

Temperature (°C)	Stress (MPa)
1100	10, 20, 30
1150	5, 10, 20
1200	5, 10, 20
1250	5, 10, 20

subjected to crystal growth process by using an optical floating zone (OFZ) furnace (model FZ-T-12,000-X-VII-VPO-PC, Crystal Systems Corporation, Japan). OFZ technique was chosen in this work in order to fabricate coarse grains with homogeneous composition [53], and samples with large grains were used to minimize the effect of grain boundary softening in HfNbTaTiZr reported in previous works [30,54,55]. The schematic drawing of the four mirror OFZ furnace used in this work is presented in Fig. 1(a). High-purity argon (99.995%) was filled inside the chamber at 101.3 kPa with 3 liters/min flux throughout the process. The pulling rate of the crystal was 15 mm/h, and the rotation rates was 3 rpm to ensure the temperature homogeneity during crystal growth.

The tensile creep specimens were manufactured by EDM, and they had a dog-bone shape with the gage-section dimensions of 5 × 2.9 × 1.5 mm³ and four ridges marking the gage-section, Fig. 1(b). The flat sides of gage were grinded by 1200 grit SiC sandpaper. The vacuum tensile creep test device was hand-built by Metals and Alloys, University of Bayreuth, details of the setup was described by earlier reports [40,56]. The device contains a graphite-heating element inside the vacuum chamber and a type-S thermocouple close to the specimen. The tensile creep tests were conducted at 1100, 1150, 1200, and 1250°C in vacuum of 2 × 10⁻⁴ Pa controlled by an oil diffusion pump. The diffusion pump ran over the whole duration of creep tests to guarantee a high vacuum level, which could prevent reaction with C, O₂, or N₂ and minimize contamination during high temperature creep tests. Two Al₂O₃ ceramic holders were used to grip the ends of the testpieces. A non-contacting video extensometer was used to record the strain evolution during creep [56]. In this work, creep tests were conducted with step-wise increase in stress; the change in load was determined by correlating the instantaneous cross-sectional area after the minimum creep rate was reached, this method was described in details by Gadelmeier et al. [49]. The tensile creep tests were conducted under stresses of 5, 10, 20, and 30 MPa, Table 1. The samples were first tested at 1100°C and 10 MPa; after the strain rate had reached the minimum creep rate, the stress was raised to 20 MPa, and then from 20 MPa to 30 MPa. The other stress change tests were also conducted with the load

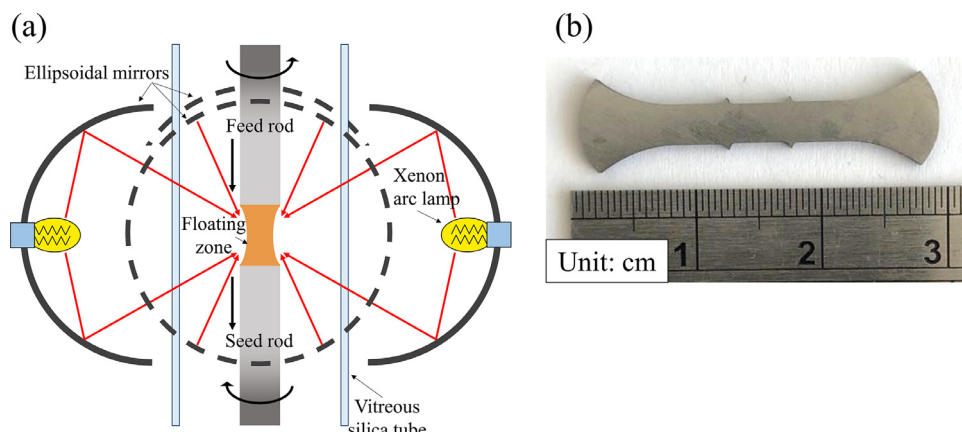


Fig. 1. (a) The schematic drawing of the optical floating zone furnace. (b) The tensile creep test specimen.

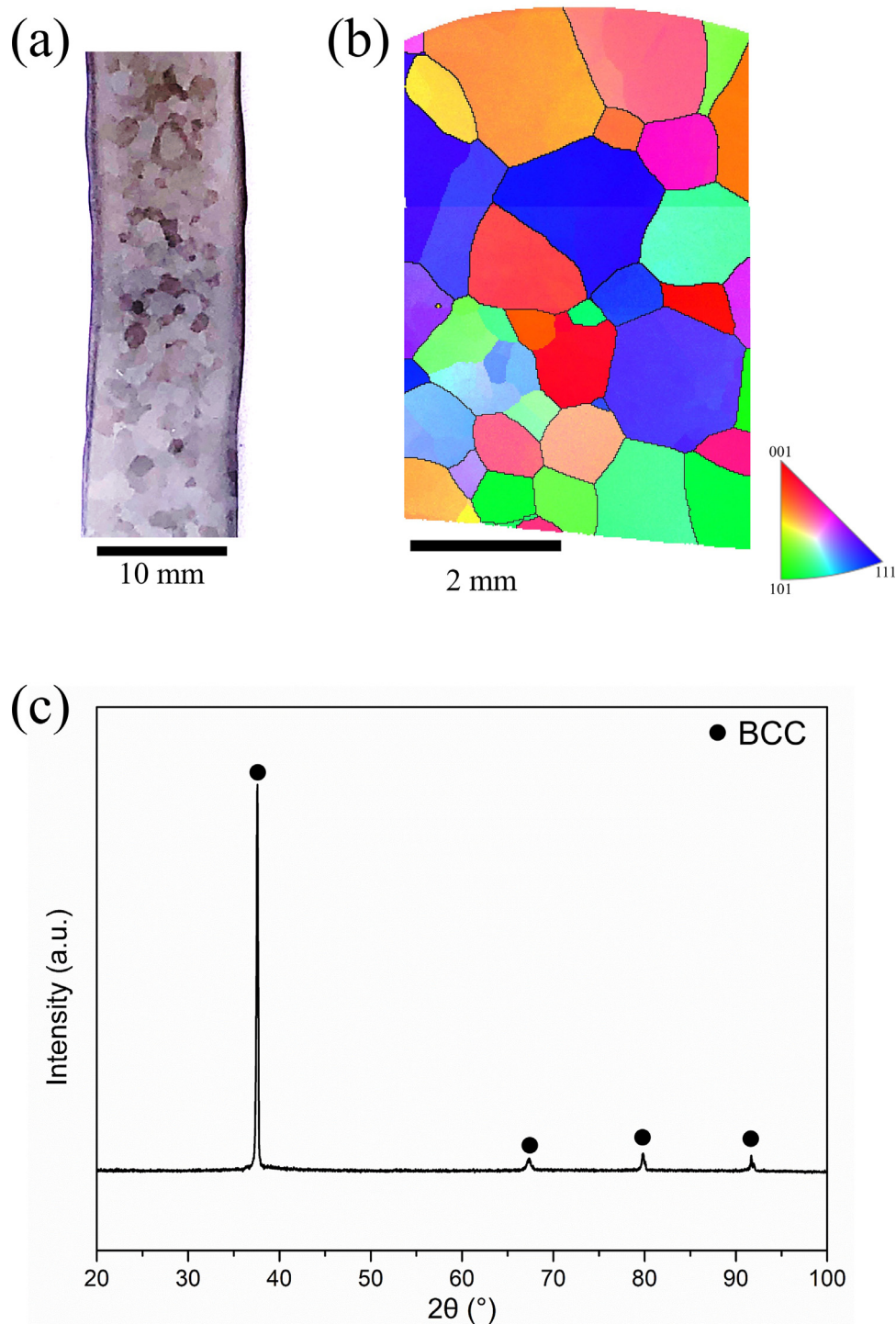


Fig. 2. (a) Longitudinal section and (b) Inverse pole figure (IPF) image of the cross section of HfNbTaTiZr. (c) X-ray diffraction pattern of sample prior creep.

increased stepwise from 5, 10 to 20 MPa at 1150°C, 1200°C, and 1250°C. The load change process took less than 2 min. After tests, all creep specimens were cooled freely to room temperature by furnace cooling. During the cooling process, from testing temperatures to 940°C, the cooling rates were about 260°C/min; from 940°C to 800°C, and 800°C to 600°C, cooling rates were 85°C/min and 32°C/min, respectively, below 600°C, the cooling was around 5–12°C/min.

To reveal the microstructures, specimen surfaces were grinded by SiC sandpaper to 4000 grit, followed by 0.05 μm Al_2O_3 and

0.02 μm silica suspension polishing steps. Etching was conducted with a hydrofluoric acid solution (20 ml hydrofluoric acid + 15 ml nitric acid + 65 ml glycerol). For grain size analysis, an optical microscope was used, and an average grain size was determined by ImageJ 1.42q [57]. X-ray diffraction (XRD, D2 PHASER X-ray diffractometer, Bruker) with $\text{Cu K}\alpha$ radiation was used to conduct phase analysis. Scanning electron microscopes (SEM, JSM-7610F, JEOL and Gemini 300, Zeiss) equipped with electron backscatter diffraction (EBSD) and energy-dispersive X-ray spectroscopy (EDS) were used to examine the microstructures in details. The backscatter Kikuchi

Table 2
The minimum creep rates of HfNbTaTiZr at different loads and temperatures.

T (°C)	Log ₁₀ minimum creep rate (s ⁻¹)							
	1100		1150		1200		1250	
Load (MPa)	Test 1	Test 2	Test 1	Test 2	Test 1	Test 2	Test 1	Test 2
5	-	-	-6.7	-6.7	-6.5	-6.5	-6.1	-6.1
10	-6.4	-6.2	-6.1	-6.0	-5.6	-5.9	-5.4	-5.3
20	-5.7	-5.6	-5.3	-5.1	-4.7	-5.0	-4.6	-
30	-5.1	-5.1	-	-	-	-	-	-

patterns were recorded by AZtec EDS/EBSD software (Oxford Instruments plc, UK) to map the misorientation profiles, and kernel average misorientation (KAM) mapping was conducted by calculating the arithmetic average of the scalar misorientation between groups of pixels [58]. Dual-beam focused ion beam (FIB, Helios Nanolab 600i, FEI, Oregon, USA) was used to prepare samples for transmission electron microscope analysis (TEM, FEI TECNAI G2 F20 TEM) operating at 200 kV. To elucidate the effects of alloying constituents in HfNbTaTiZr on creep rates, thermodynamic database TCHEA4 and mobility database MOBHEA2 were used to estimate the intrinsic diffusivities of each element in the system, so the theoretical creep rates could be determined to compare with those of experimental values for discussion.

3. Results and analysis

3.1. Microstructure prior creep

The sample of HfNbTaTiZr processed by OFZ furnace had an average grain size of 1.2 ± 0.4 mm, Fig. 2(a) and 2(b), and this was substantially coarser than the grain sizes of this RHEA reported in previous works fabricated by arc-melting (140 μm) [54], spark plasma sintering (20–190 μm) [59,60], and hot isostatic pressing (100–200 μm) [29,30]. The microstructure of the sample exhibited a BCC single phase with a lattice parameter of 340 pm, Fig. 2(c). There was no dendritic segregation observed and the equi-atomic compositions of HfNbTaTiZr was confirmed by SEM-EDS.

3.2. Creep behavior

Creep curves are shown in Fig. 3(a), and the evolutions of creep rates versus creep strain are shown in Fig. 3(b). All creep curves exhibit minimal primary creep strains, and creep deformations under all conditions were dominated by obvious steady state creep regions. The coarse grains structure fabricated by OFZ technique was to minimize the grain boundary softening, so the intrinsic creep mechanism of HfNbTaTiZr could be elucidated. Although the texture of coarse grains has been known to influence creep strains and creep lives [61], this study focused on elucidating creep mechanism based on the minimum creep strain rates. The minimum creep rates have been determined and summarized in Table 2. Creep tests under each condition were performed twice to ensure reproducibility, the minimum creep rates of two sets of tests were almost the same under the same stress and temperature. So, this indicates that the use of coarse grain structure of HfNbTaTiZr in this work could result consistent minimum creep strain rates under present testing conditions.

The minimum creep rate can be used to determine the stress exponent n and the creep activation energy Q from the power-law equation [62]:

$$\dot{\epsilon}_{min} = A\sigma^n \exp\left(-\frac{Q}{RT}\right) \quad (3-1)$$

Table 3
Calculated power-law parameters, n , Q and coefficients of determination R^2 .

T (°C)	n	R ²
1100	2.5	0.9747
1150	2.5	0.9820
1200	2.8	0.9600
1250	2.5	0.9968
Stress (MPa)	Q (kJ mol ⁻¹)	R ²
5	259	0.9147
10	258	0.8979
20	288	0.9380

where $\dot{\epsilon}_{min}$ is the minimum creep rate, A is a material specific constant, σ is the applied stress, R is the gas constant, and T is the absolute temperature.

By plotting the minimum creep rates against the applied stresses, Fig. 4(a), values of the stress exponent n can be determined from slopes of linear regression lines. The activation energy Q for creep can be determined by plotting the natural log of the minimum creep rate at a specific stress versus the reciprocal of temperature, Fig. 4(b). The values of n and Q and their standard deviations are summarized in Table 3. The stress exponent values in this work vary in the range of 2.5 to 2.8, which suggests the solute drag creep mechanism [63,64], and the activation energy is determined to be 273 ± 15 kJ mol⁻¹. There was no transition between different creep mechanisms within the stresses and temperatures regime in this investigation.

3.3. Microstructures after creep

The microstructure of crept HfNbTaTiZr evolved significantly after deformation, Fig. 5; grain morphology was distinctly different from the microstructure prior creep shown in Fig. 2. Fig. 5 shows that significant bulging of grain boundaries occurred during creep, and these bulging grain boundaries were associated with high levels of misorientation, which indicates concentration of deformation in the vicinity of grain boundaries. This type of deformed grain boundaries in HfNbTaTiZr was reported previously during the early stage of uniaxial compression testing at 1000°C [55], and continuing deformation under compression to over 30% would lead to dynamic recrystallization in necklace form along initial grain boundaries [30,54,55]. However, the necklace structure at boundaries was not identified after creep in this study, Fig. 5. Furthermore, sub-grain boundaries were observed near bulging grain boundaries due to polygonization, Fig. 5(c, f, i, l), this phenomena was observed in other metals deformed in the solute drag regime [65,66]. Despite significant deformation of grain boundaries after creep, there was no crack or void observed at the intergranular regions.

To further examine the crept microstructures, TEM images were analyzed. Since all creep conditions from 1100 to 1250 °C shared similar deformation behavior and stress exponent values, the dislocation structures of HfNbTaTiZr after creep at 1100 °C/30 MPa with

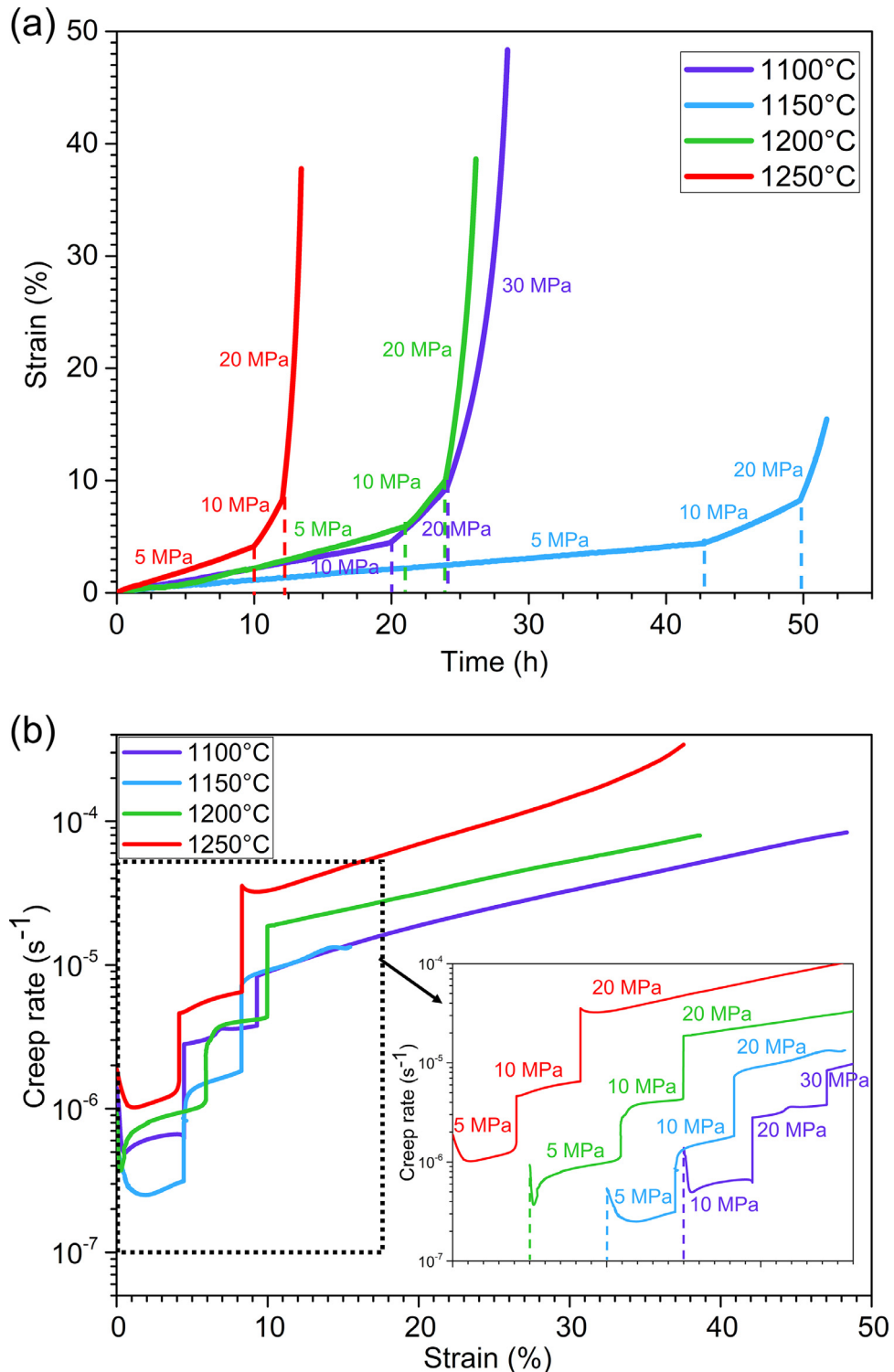


Fig. 3. (a) Tensile creep curves, (b) Creep rate versus strain.

48% strain are shown exemplarily in this work, Fig. 6. The dislocations were randomly distributed, and they were long and neatly arranged without entanglement. There were also dislocation accumulation along the grain boundaries, Fig. 6(b), the selected area diffraction patterns confirmed that deformed HfNbTaTiZr still retained its BCC structure, exemplified by the [011] zone axis. In addition, the Burger's vector (b) of the gliding dislocations was determined by TEM analysis with the $g \cdot b$ invisibility criterion. The dislocations were visible with $\bar{g} = [2\bar{1}\bar{1}]$ in Fig. 6(d), while they were

out of contrast with $\bar{g} = [2\bar{1}\bar{1}]$ in Fig. 6(e) and $\bar{g} = [01\bar{1}]$ in Fig. 6(f). This analysis has validated that dislocations in tensile creep deformed HfNbTaTiZr were $a/2<111>$ type.

4. Discussion

The stress exponent n can be used to elucidate the dominant creep mechanism. For HfNbTaTiZr tested at 1100–1250 °C and 5–30 MPa, the stress exponents were in-between 2.5–2.8, which is

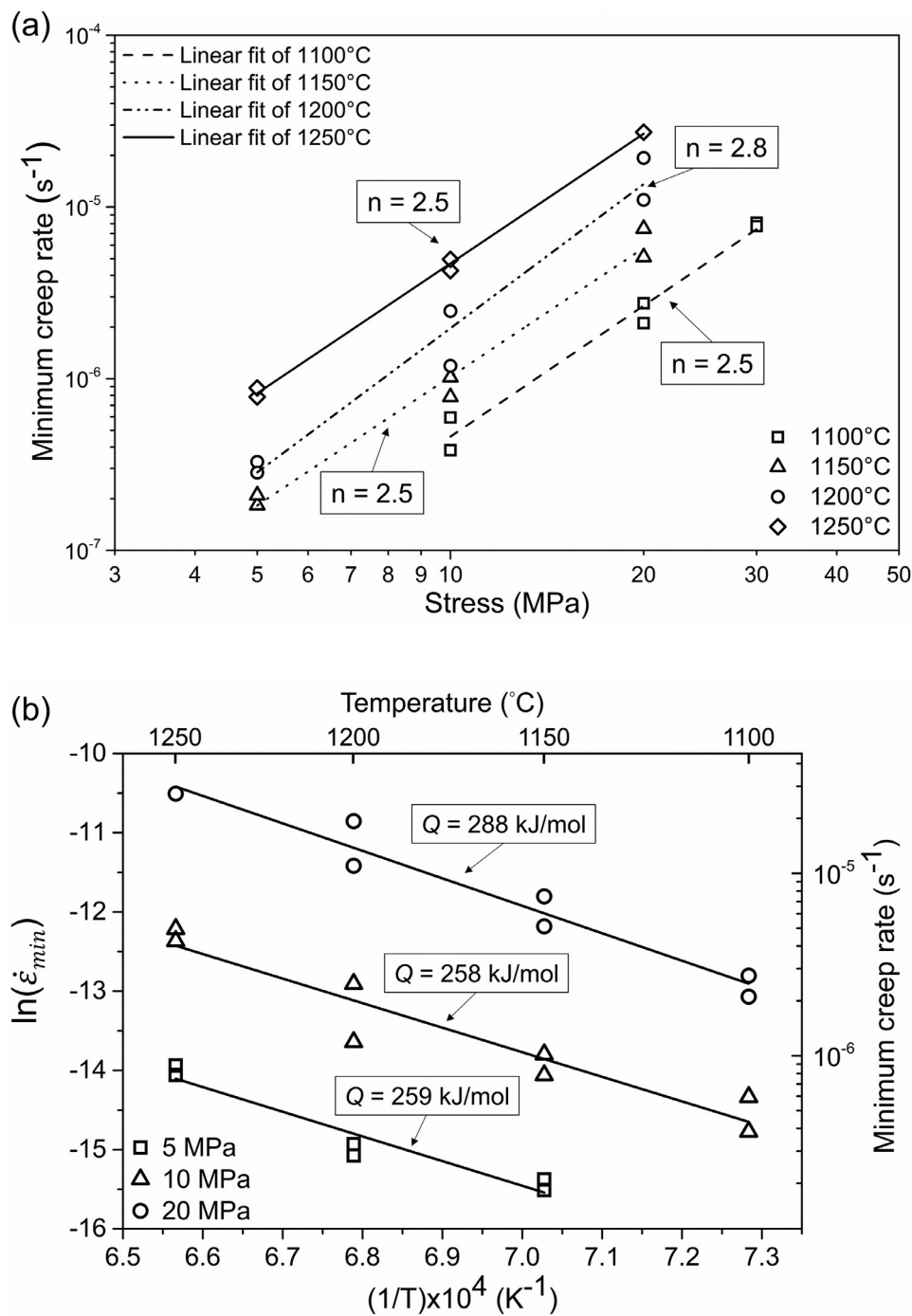


Fig. 4. (a) Minimum creep rates versus applied stress from 1100 to 1250 °C, (b) minimum creep rates versus the reciprocal of the absolute temperatures from 5 to 20 MPa.

slightly lower than 3. The stress exponent about 3 is known to be related to solute drag creep (viscous glide creep or the Class I solid solution creep behavior), and solute drag creep is often observed for solid solution alloys [63,64]. The solute drag creep effect can additionally be raised from dislocation interactions with solute atoms and retard dislocation glide movement [62,64,67–69]. Furthermore, a transition from solute drag creep to climb-controlled creep would be observed with the breakaway of dislocations from the stress field of solute with higher stresses [63]. Since the stress exponents determined from all creep conditions were similar, the creep mechanism did not change within different temperatures and stresses in this study. This indicates that the stress level

in this work was not high enough to overcome the solute drag effect.

In addition to the stress exponent, the microstructures after creep in Fig. 6 also suggest solute drag creep in present study. Since the completion of creep tests were followed by sufficient cooling rate ($\sim 260 \text{ }^\circ\text{C}/\text{min}$ from testing temperatures to $940 \text{ }^\circ\text{C}$), the dislocation structures would be retained after creep tests. The observed dislocations were slightly curved without entanglement; this observation is typically identified in samples deformed by solute drag mechanism [46,63,65].

Bulging grain boundaries and vast levels of misorientation along grain boundaries after creep, Fig. 5, have been shown by KAM anal-

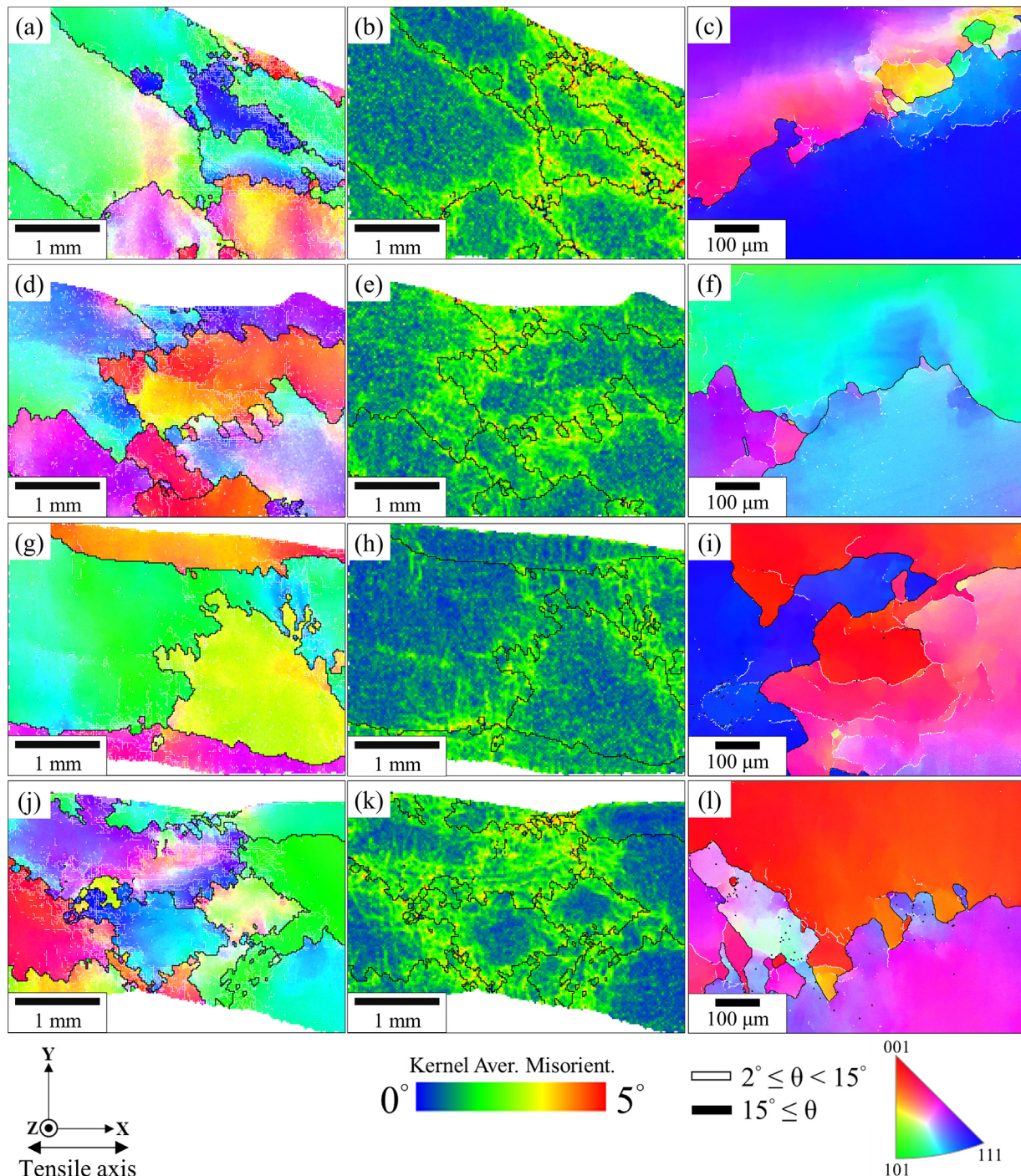


Fig. 5. SEM-EBSD images of the specimens after creep under different temperatures: (a, b, c) 1100°C, (d, e, f) 1150°C, (g, h, i) 1200°C and (j, k, l) 1250°C; (a, d, g, j) are inverse pole figure maps, (b, e, h, k) are kernel average misorientation maps and (c, f, i, l) are inverse pole figure maps under higher magnification.

ysis. Based on the deduced creep mechanism, the grains were deformed by dislocations, Fig. 6, dislocations piling up at the grain boundaries were also observed, Fig. 6(b) and (c). The variation of dislocation densities at grain boundaries activated the bulging of grain boundaries at different segments, which is known as the strain induced grain boundary migration [55,70]. The evolution of microstructure of HfNbTaTiZr after deformation in this work is different from those reported previously [30,54,55]. In the work conducted by Senkov et al. [30], dynamic recrystallization was observed after deformation; HfNbTaTiZr with initial grain size of 100–200 μm was subjected to 50% height reduction under compression

at temperatures up to 1200°C, the strain rate was 10^{-3} s^{-1} and the stress could reach 92 MPa and above. Eleti et al. [54] also reported dynamic recrystallization of 50% height reduction hot-compressed HfNbTaTiZr with an average initial grain size of 140 μm, the strain rate was 10^{-4} s^{-1} and the stress could reach 44 MPa and above. The evolution of microstructure under compression was further clarified in another work by Eleti et al. [55]; with the strain rate of 10^{-3} s^{-1} , bulging grain boundaries associated with strain induced grain boundary migration were observed during the early stage of compression deformation under 10% strain at 1000°C, and there was no dynamic recrystallization reported until 30% reduction. The

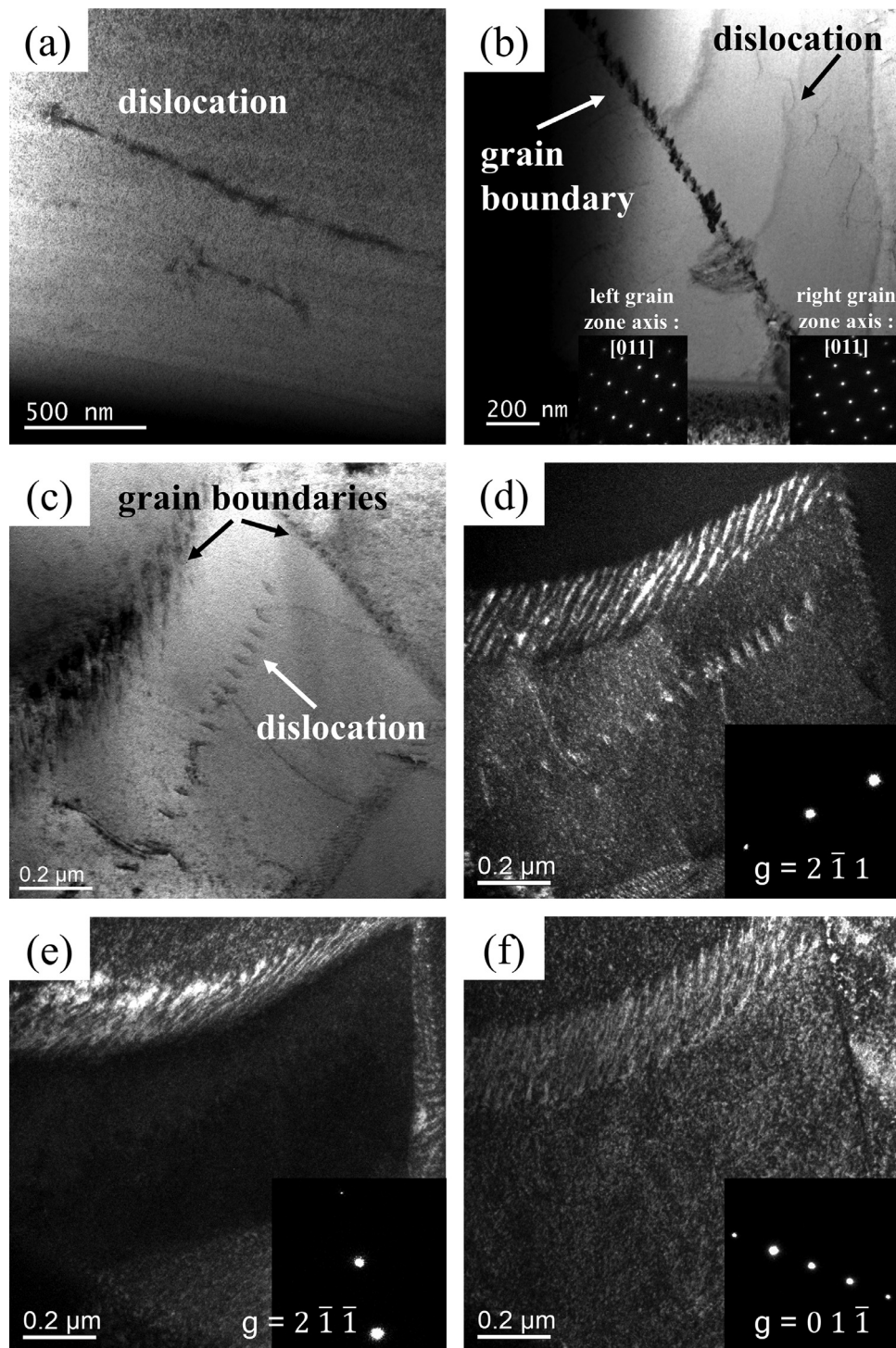


Fig. 6. TEM images of HfNbTaTiZr after creep at 1100 °C. (a) dislocation structure within grain interior; (b, c) overview of dislocation and grain boundary structure after creep; (d, e, f) Weak-beam dark-field micrographs from the same area of (c) in zone axis near (d) $[1\bar{1}\bar{3}]$, (e) $[1\bar{3}\bar{1}]$ and (f) $[1\bar{1}\bar{1}]$.

dynamic recrystallization in those compression tests could evolve from around the initial grain boundaries in necklace form to fully recrystallization with reduction ratios greater than 30%. By contrast, the mode of deformation in this work was creep in tension under relatively lower stresses (5–30 MPa), with creep strains of 15 to 48% and above, the stress build-up at the grain boundaries should be lower than those subjected to compression deformation [30,54,55], hence bulging grain boundaries were observed with no dynamic recrystallization, Fig. 5. Furthermore, the grain size in this

work (1.2 ± 0.4 mm) was about 10 times larger than those of Senkov et al. [30] and Eleti et al. [54], so deformation attributed to diffusion along grain boundary can be less. Hence the tensile creep activation energy (273 ± 15 kJ mol⁻¹) determined in the present work is higher than the activation energies of compression deformation reported by Senkov et al. [30] (226 ± 20 kJ mol⁻¹) and Eleti et al. [54] (245 ± 13 kJ mol⁻¹).

All our observations highlight that the tensile creep mechanism of HfNbTaTiZr at elevated temperatures is glide-controlled creep by

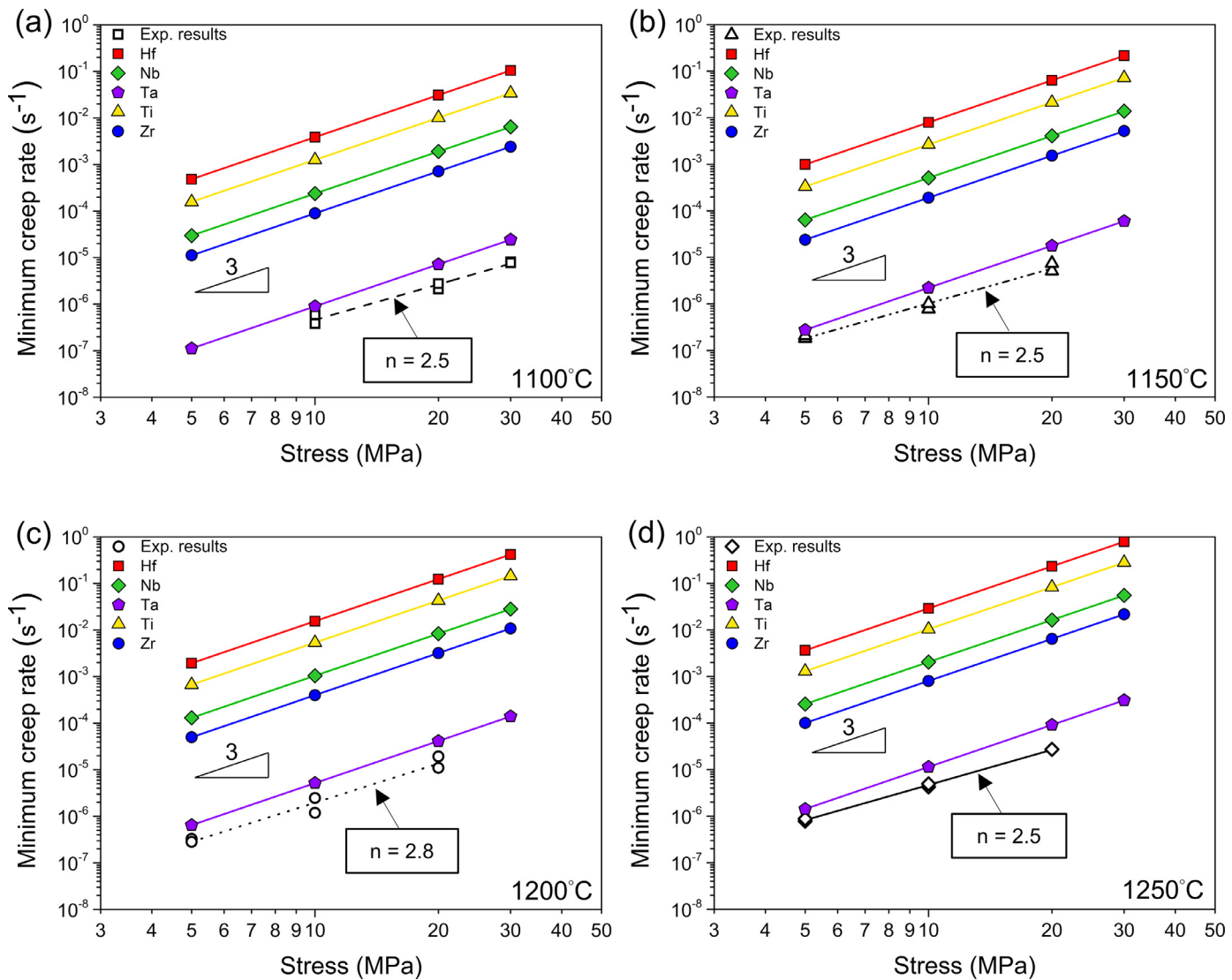


Fig. 7. The minimum creep rates against applied stress for the experimental work and the calculated ones at (a) 1100 °C, (b) 1150 °C, (c) 1200 °C and (d) 1250 °C.

solute drag. This can also refer to the case in which dislocations encounter frictional stress acting on it by dragging the solute stress fields [63,64,71]. According to Mohamed et al. [64], the minimum creep rate can be modeled using the following equation:

$$\dot{\varepsilon}_{min} = \frac{\pi(1-\nu)\sigma^3}{6AG^2} \quad (4-1)$$

where ν is the Poisson's ratio, σ is the applied stress, G is shear modulus of the alloy, and A represents the interaction of dislocations with solute atoms which is expressed as Eq. (4-2) according to Cottrell et al. [71]:

$$A = \frac{e^2 cb^5 G^2}{kT\tilde{D}} \quad (4-2)$$

where e is the solute-solvent size difference, c is the concentration of solute atoms, b is Burger's vector, k is Boltzmann's constant, T is the absolute temperature, and \tilde{D} is the diffusion coefficient of solute atoms. Combining Eqs. (4-1) and (4-2) can give the following expression to predict the minimum creep rate [63]:

$$\dot{\varepsilon}_{min} = \frac{\pi(1-\nu)kT\tilde{D}}{6e^2 cb^5 G} \left(\frac{\sigma}{G} \right)^3 \quad (4-3)$$

According to solute drag by the Cottrell-Jaswon mechanism (Eq. (4-3)), the dislocation could drift under the action of stress acting

on it by dragging behind it a solute atmosphere [71]. The solute atmosphere could travel by means of the diffusion of the solute atoms. If the dislocation was to move at a given velocity, then the solute atoms must diffuse at the same velocity [63]. Although Eq. (4-3) has been commonly used in conventional alloys, Kim et al. [45] adopted this equation by considering each constituent as the solute atmosphere and made a direct comparison between the calculated values and the observed minimum creep rates. The results suggested that the solute drag of Ni controlled the viscous glide during creep of CoCrFeMnNi. Therefore, this work has applied the same approach to determine the solute which would dominate the dragging mechanism during creep of HfNbTaTiZr. However, what should be the appropriate diffusion coefficients, \tilde{D} , of HfNbTaTiZr for Eq. (4-3)? Even though a similar question was previously discussed in binary systems [64,72–76], this has remained an issue of debate. In concentrated multicomponent solid solutions, the determination of the appropriate diffusion coefficient can be even more challenging. Heckl et al. [77] tackled the problem in Ni-based superalloys and considered the weighted harmonic mean of the diffusion coefficients of alloying constituents by referring to the treatments from Herring [72] and Reed et al. [78]. However, these different authors considered three different diffusion coefficients, i.e., intrinsic, tracer, or chemical diffusion coefficients, which can be

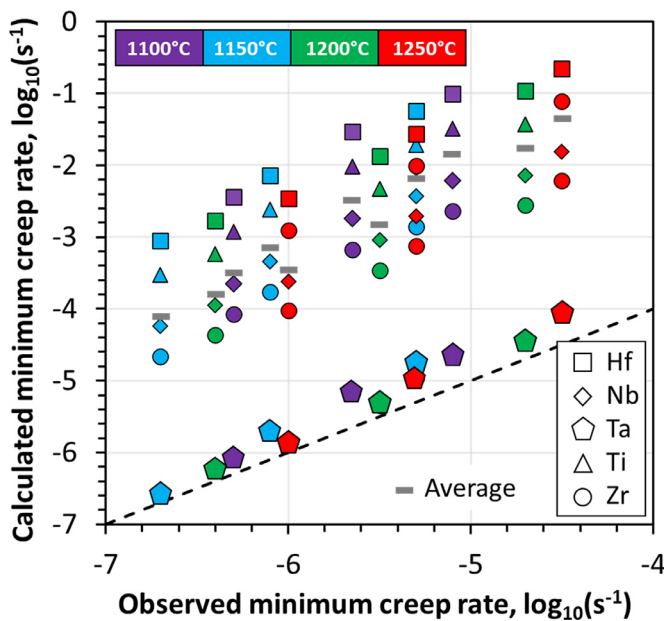


Fig. 8. Predicted vs observed minimum creep rates at 1100, 1150, 1200 and 1250 °C and for three different applied stresses between 5 and 30 MPa.

questionable in this approach. Besides, the invoked Herring's equation [72] is valid for climb-controlled creep only, not glide. A diffusion coefficient is, by definition, the proportionality factor between the flux and the concentration gradient. In a 5-components system, the flux equations give a 4×5 intrinsic diffusivity matrix (in the lattice-fixed frame of reference) to describe the diffusion process. To simplify this complicated problem, cross terms can be neglected by postulating small concentration gradients between the segregation surrounding the dislocation and the concentrated solid solution matrix. Only five intrinsic (individual) diffusion coefficients are then sufficient, so the observed minimum creep rates with those inferred from the individual diffusion coefficient of each constitutive element using Eq. (4–3) can be compared and determine possible elemental effects. Table 4 provides the parameters required to calculate the minimum creep rates by Eq. (4–3). The composition and temperature dependencies of diffusivities for individual elements in HfNbTaTiZr have been computed using the thermo-

Table 4

The values of intrinsic diffusion coefficients (D_i) for individual elements in HfNbTaTiZr calculated at different temperatures using ThermoCalc and the TCHEA4 and MOBHEA2 databases, atomic radius (r) [80,81] and solute-solvent size difference (e).

	Hf	Nb	Ta	Ti	Zr
Intrinsic diffusion coefficients, $\log_{10}(m^2/s)$					
1100 °C	-12.3	-13.6	-16.0	-13.4	-13.7
1150 °C	-12.0	-13.3	-15.7	-13.1	-13.4
1200 °C	-11.7	-13.0	-15.3	-12.8	-13.1
1250 °C	-11.5	-12.7	-15.0	-12.5	-12.8
Atomic radius					
r (pm)	157.8	142.9	143.0	146.2	160.3
Solute-solvent size difference					
e (%)	+5.2	-4.8	-4.7	-2.6	+6.8

dynamic TCHEA4 and mobility MOBHEA2 database. The calculated diffusion coefficient of Zr in HfNbTaTiZr at 1150 °C in this work is similar to an experimental result reported recently by Zhang et al. [79].

The size difference of each element (e_i) can be determined from the following equation [45]:

$$e_i = \frac{r_i - r_{average}}{r_{average}} \quad (4-4)$$

where r_i is the radius of the element of i , and $r_{average}$ is the average radius of the constituent atoms according to atomic fraction (X_i) of HfNbTaTiZr ($\sum_{i=1}^5 X_i r_i$).

The shear modulus of HfNbTaTiZr has been estimated to vary from 30 to 28 GPa between 1100 and 1250 °C according to $G = 36.2 - 5.6/(e^{845/T} - 1)$ [82]. The value of 0.26 for the Poisson's ratio can be taken from previous work [82], and the Burger's vector can be calculated from the lattice constant in Fig. 2(c), $b = a/2<111> = 0.294$ nm. The minimum creep rates can then be calculated at 1100, 1150, 1200 and 1250 °C by considering each intrinsic diffusion coefficient separately. The results are illustrated in Fig. 7.

The calculated minimum creep rates in Fig. 7 shows that $\dot{\epsilon}_{min-Ta} < \dot{\epsilon}_{min-Zr} < \dot{\epsilon}_{min-Nb} < \dot{\epsilon}_{min-Ti} < \dot{\epsilon}_{min-Hf}$. Although the experimental results plotted in Fig. 7 are slightly slower than the $\dot{\epsilon}_{min-Ta}$, it is very similar to the calculated results based on the intrinsic diffusion of Ta in HfNbTaTiZr, under all stresses and temperatures. Fig. 8 shows that taking the harmonic average of the

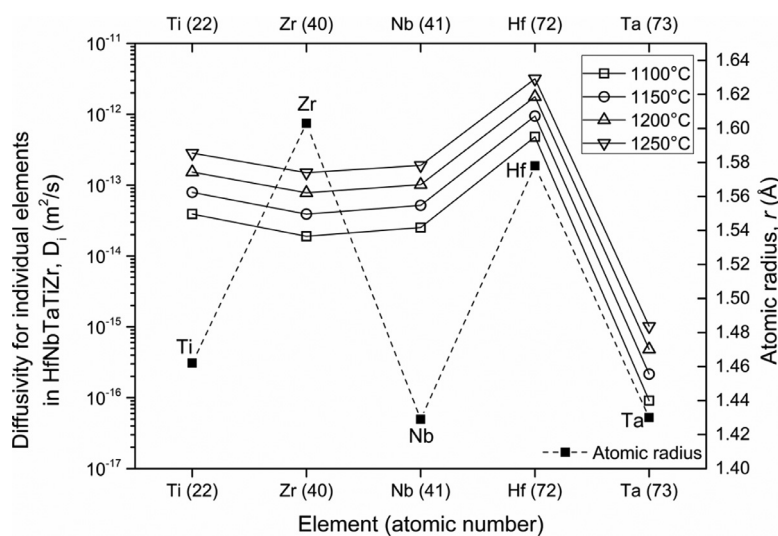


Fig. 9. Diffusivity and atomic radius [80,81] for each element in HfNbTaTiZr RHEA.

intrinsic diffusion coefficients in Eq. (4–3) does not agree with the experimentally determined minimum creep rate. In contrast, the minimum creep rate is predicted with a good agreement with experimental observations using the intrinsic diffusion coefficient of Ta, which indicates that Ta contributes the most to drag dislocations during creep in HfNbTaTiZr.

The diffusion rate in alloy systems is generally believed to be lower when the solute-solvent size difference of individual elements is larger [83]. However, in Fig. 9, the diffusivity for individual elements in HfNbTaTiZr from calculation disproves this traditional view. Table 4 shows that Zr and Hf have larger atomic radii, but the diffusivities are faster than Ta in several orders of magnitude. Instead, although Ta does not contribute to the highest size differences, the result implies that the solute drag effect is more dependent on the diffusivity, and Ta has the lowest diffusion coefficients in HfNbTaTiZr and therefore contributes the most to drag dislocations. A similar phenomenon was reported in nickel-base superalloy [84,85]; Re and Ru have slower diffusion rates in Ni than Zr and Hf, albeit Zr and Hf possess greater atomic radii than Re and Ru, this behavior is thought to be related to the bonding characteristics of solute atoms. Furthermore, the diffusivity is affected by both the thermodynamic factor and the atomic mobility, and low mobility generally comes with a high melting point; the high melting point of Ta may play a role in the observed solute drag creep. Future experimental studies of interdiffusion, solute-vacancy exchange and bonding characteristics in HfNbTaTiZr can help to further understand its high temperature properties. And, single crystals of HfNbTaTiZr would help to further clarify the effect of crystal orientation on deformation behaviors. To our knowledge, this work is the first to unveil the creep deformation mechanism of HfNbTaTiZr in tension, especially up to 1250°C.

5. Conclusion

The current work investigated creep behaviors of HfNbTaTiZr with large grain size fabricated by the optical floating zone technique. Creep properties and microstructure were examined for samples tested at 1100–1250°C and stress levels of 5–30 MPa under vacuum. The important findings are listed as follows.

- (1) The creep behavior was related to the solute drag mechanism, which is evidenced by the stress exponents of 2.5–2.8. The creep activation energies obtained in this work are in the range of $273 \pm 15 \text{ kJ mol}^{-1}$.
- (2) TEM characterization has verified that plasticity of creep was dominated by dislocations of $b = a/2<111>$.
- (3) Dislocations at grain boundaries have led to significant bulging of grain boundaries associated with strain-induced grain boundary migration.
- (4) According to the diffusivity calculation and solute drag creep model prediction, the creep rates were controlled by diffusivity of Ta, which is the element with the lowest diffusion coefficient in HfNbTaTiZr and suppresses dislocation movement during creep.

These findings can be applied to design advanced RHEAs to improve the creep rate and related rapture.

Declaration of Competing Interest

The authors declare that they have no known competing financial interests or personal relationships that could have appeared to influence the work reported in this paper.

Acknowledgment

This work was supported by the “High Entropy Materials Centre” from The Featured Areas Research Centre Program within

the framework of the Higher Education Sprout Project by the Ministry of Education (MOE) and from the project by Ministry of Science and Technology (MOST) in Taiwan [MOST107-2923-E-007-010-MY3, MOST110-2927-I-007-512, MOST111-2634-F-007-008, MOST111-2224-E-007-003, MOST110-2221-E-007-020-MY3]; The group of Metals and Alloys of the University of Bayreuth was supported by the Deutsche Forschungsgemeinschaft (DFG) with project GL 181/56-2 and the priority programme SPP2006 “Compositionally Complex Alloys - High Entropy Alloys (CCA-HEA)”. SG gratefully acknowledges the support by the CNRS through the 80 PRIME programme.

References

- [1] J.W. Yeh, S.K. Chen, S.J. Lin, J.Y. Gan, T.S. Chin, T.T. Shun, C.H. Tsau, S.Y. Chang, Nanostructured high-entropy alloys with multiple principal elements: novel alloy design concepts and outcomes, *Adv. Eng. Mater.* 6 (5) (2004) 299–303, doi:[10.1002/adem.200300567](https://doi.org/10.1002/adem.200300567).
- [2] B. Cantor, I.T.H. Chang, P. Knight, A.J.B. Vincent, Microstructural development in equiatomic multicomponent alloys, *Mater. Sci. Eng. A* 375–377 (2004) 213–218, doi:[10.1016/j.msea.2003.10.257](https://doi.org/10.1016/j.msea.2003.10.257).
- [3] D.B. Miracle, O.N. Senkov, A critical review of high entropy alloys and related concepts, *Acta Mater.* 122 (2017) 448–511, doi:[10.1016/j.actamat.2016.08.081](https://doi.org/10.1016/j.actamat.2016.08.081).
- [4] M.-H. Tsai, J.-W. Yeh, High-entropy alloys: a critical review, *Mater. Res. Lett.* 2 (3) (2014) 107–123, doi:[10.1080/21663831.2014.912690](https://doi.org/10.1080/21663831.2014.912690).
- [5] S. Gorse, J.-P. Couzinié, D.B. Miracle, From high-entropy alloys to complex concentrated alloys, *C.R. Phys.* 19 (8) (2018) 721–736, doi:[10.1016/j.crhy.2018.09.004](https://doi.org/10.1016/j.crhy.2018.09.004).
- [6] X. Yang, Y. Zhang, Prediction of high-entropy stabilized solid-solution in multi-component alloys, *Mater. Chem. Phys.* 132 (2) (2012) 233–238, doi:[10.1016/j.matchemphys.2011.11.021](https://doi.org/10.1016/j.matchemphys.2011.11.021).
- [7] Y. Zhang, Y.J. Zhou, J.P. Lin, G.L. Chen, P.K. Liaw, Solid-solution phase formation rules for multi-component alloys, *Adv. Eng. Mater.* 10 (6) (2008) 534–538, doi:[10.1002/adem.200700240](https://doi.org/10.1002/adem.200700240).
- [8] F.G. Courty, M. Kaufman, A.J. Clarke, Solid-solution strengthening in refractory high entropy alloys, *Acta Mater.* 175 (2019) 66–81, doi:[10.1016/j.actamat.2019.06.006](https://doi.org/10.1016/j.actamat.2019.06.006).
- [9] K. Ming, X. Bi, J. Wang, Strength and ductility of CrFeCoNiMo alloy with hierarchical microstructures, *Int. J. Plast.* 113 (2019) 255–268, doi:[10.1016/j.ijplas.2018.10.005](https://doi.org/10.1016/j.ijplas.2018.10.005).
- [10] M.N. Hasan, Y.F. Liu, X.H. An, J. Gu, M. Song, Y. Cao, Y.S. Li, Y.T. Zhu, X.Z. Liao, Simultaneously enhancing strength and ductility of a high-entropy alloy via gradient hierarchical microstructures, *Int. J. Plast.* 123 (2019) 178–195, doi:[10.1016/j.ijplas.2019.07.017](https://doi.org/10.1016/j.ijplas.2019.07.017).
- [11] Y.-T. Chen, Y.-J. Chang, H. Murakami, T. Sasaki, K. Hono, C.-W. Li, K. Kakehi, J.-W. Yeh, A.-C. Yeh, Hierarchical microstructure strengthening in a single crystal high entropy superalloy, *Sci. Rep.* 10 (1) (2020) 12163, doi:[10.1038/s41598-020-69257-8](https://doi.org/10.1038/s41598-020-69257-8).
- [12] S. Gorse, Y.-T. Chen, W.-C. Hsu, H. Murakami, A.-C. Yeh, Modeling the precipitation processes and the formation of hierarchical microstructures in a single crystal high entropy superalloy, *Scr. Mater.* 193 (2021) 147–152, doi:[10.1016/j.scriptamat.2020.11.002](https://doi.org/10.1016/j.scriptamat.2020.11.002).
- [13] A.-C. Yeh, Y.-J. Chang, C.-W. Tsai, Y.-C. Wang, J.-W. Yeh, C.-M. Kuo, On the solidification and phase stability of a Co-Cr-Fe-Ni-Ti high-entropy alloy, *Metall. Mater. Trans. A* 45 (1) (2014) 184–190, doi:[10.1007/s11661-013-2097-9](https://doi.org/10.1007/s11661-013-2097-9).
- [14] T.-T. Shun, L.-Y. Chang, M.-H. Shiu, Microstructures and mechanical properties of multiprincipal component CoCrFeNiTi alloys, *Mater. Sci. Eng. A* 556 (2012) 170–174, doi:[10.1016/j.msea.2012.06.075](https://doi.org/10.1016/j.msea.2012.06.075).
- [15] Y.-J. Chang, A.-C. Yeh, The evolution of microstructures and high temperature properties of Al_xCo_{1.5}Cr_yFe_{1.5}Ti_{0.5} high entropy alloys, *J. Alloys Compd.* 653 (2015) 379–385, doi:[10.1016/j.jallcom.2015.09.042](https://doi.org/10.1016/j.jallcom.2015.09.042).
- [16] Y. Wang, S. Ma, X. Chen, J. Shi, Y. Zhang, J. Qiao, Optimizing mechanical properties of AlCoCrFeNiTi high-entropy alloys by tailoring microstructures, *Acta Metall. Sin. (Engl. Lett.)* 26 (3) (2013) 277–284, doi:[10.1007/s40195-012-0174-5](https://doi.org/10.1007/s40195-012-0174-5).
- [17] Y.J. Zhou, Y. Zhang, Y.L. Wang, G.L. Chen, Solid solution alloys of AlCoCrFeNiTi with excellent room-temperature mechanical properties, *Appl. Phys. Lett.* 90 (18) (2007) 181904, doi:[10.1063/1.2734517](https://doi.org/10.1063/1.2734517).
- [18] K. Ming, X. Bi, J. Wang, Realizing strength-ductility combination of coarse-grained Al_{0.2}Co_{1.5}Cr_yFe_{1.5}Ti_{0.3} alloy via nano-sized, coherent precipitates, *Int. J. Plast.* 100 (2018) 177–191, doi:[10.1016/j.ijplas.2017.10.005](https://doi.org/10.1016/j.ijplas.2017.10.005).
- [19] F. He, Z. Yang, S. Liu, D. Chen, W. Lin, T. Yang, D. Wei, Z. Wang, J. Wang, J.-j. Kai, Strain partitioning enables excellent tensile ductility in precipitated heterogeneous high-entropy alloys with gigapascal yield strength, *Int. J. Plast.* 144 (2021) 103022, doi:[10.1016/j.ijplas.2021.103022](https://doi.org/10.1016/j.ijplas.2021.103022).
- [20] B. Gwalani, S. Gorse, D. Choudhuri, Y. Zheng, R.S. Mishra, R. Banerjee, Tensile yield strength of a single bulk Al_{0.3}CoCrFeNi high entropy alloy can be tuned from 160 MPa to 1800 MPa, *Scr. Mater.* 162 (2019) 18–23, doi:[10.1016/j.scriptamat.2018.10.023](https://doi.org/10.1016/j.scriptamat.2018.10.023).
- [21] A. Manzoni, H. Daoud, R. Völkl, U. Glatzel, N. Wanderka, Phase separation in equiatomic AlCoCrFeNi high-entropy alloy, *Ultramicroscopy* 132 (2013) 212–215, doi:[10.1016/j.ultramic.2012.12.015](https://doi.org/10.1016/j.ultramic.2012.12.015).

- [22] S. Haas, A.M. Manzoni, M. Holzinger, U. Glatzel, Influence of high melting elements on microstructure, tensile strength and creep resistance of the compositionally complex alloy Al10Co25Cr8Fe15Ni36Ti6, *Mater. Chem. Phys.* 274 (2021) 125163, doi:[10.1016/j.matchemphys.2021.125163](https://doi.org/10.1016/j.matchemphys.2021.125163).
- [23] A.C. Yeh, T.K. Tsao, Y.J. Chang, K.C. Chang, J.W. Yeh, M.S. Chiou, S.R. Jian, C.M. Kuo, W.R. Wang, H. Murakami, Developing new type of high temperature alloys-high entropy superalloys, *Int. J. Metall. Mater. Eng.* 1 (107) (2015) 1–4, doi:[10.15344/2455-2372/2015/107](https://doi.org/10.15344/2455-2372/2015/107).
- [24] T.-K. Tsao, A.-C. Yeh, H. Murakami, The microstructure stability of precipitation strengthened medium to high entropy superalloys, *Metall. Mater. Trans. A* 48 (5) (2017) 2435–2442, doi:[10.1007/s11661-017-4037-6](https://doi.org/10.1007/s11661-017-4037-6).
- [25] O.N. Senkov, D. Isheim, D.N. Seidman, A.L. Pilchak, Development of a refractory high entropy superalloy, *Entropy* 18 (3) (2016), doi:[10.3390/e18030102](https://doi.org/10.3390/e18030102).
- [26] O.N. Senkov, G.B. Wilks, D.B. Miracle, C.P. Chuang, P.K. Liaw, Refractory high-entropy alloys, *Intermetallics* 18 (9) (2010) 1758–1765, doi:[10.1016/j.intermet.2010.05.014](https://doi.org/10.1016/j.intermet.2010.05.014).
- [27] S. Gorsse, D.B. Miracle, O.N. Senkov, Mapping the world of complex concentrated alloys, *Acta Mater.* 135 (2017) 177–187, doi:[10.1016/j.actamat.2017.06.027](https://doi.org/10.1016/j.actamat.2017.06.027).
- [28] O.N. Senkov, G.B. Wilks, J.M. Scott, D.B. Miracle, Mechanical properties of Nb25Mo25Ta25W25 and V20Nb20Mo20Ta20W20 refractory high entropy alloys, *Intermetallics* 19 (5) (2011) 698–706, doi:[10.1016/j.intermet.2011.01.004](https://doi.org/10.1016/j.intermet.2011.01.004).
- [29] O.N. Senkov, J.M. Scott, S.V. Senkova, D.B. Miracle, C.F. Woodward, Microstructure and room temperature properties of a high-entropy TaNbHfZrTi alloy, *J. Alloys Compd.* 509 (20) (2011) 6043–6048, doi:[10.1016/j.jallcom.2011.02.171](https://doi.org/10.1016/j.jallcom.2011.02.171).
- [30] O.N. Senkov, J.M. Scott, S.V. Senkova, F. Meisenkothen, D.B. Miracle, C.F. Woodward, Microstructure and elevated temperature properties of a refractory TaNbHfZrTi alloy, *J. Mater. Sci.* 47 (9) (2012) 4062–4074, doi:[10.1007/s10853-012-6260-2](https://doi.org/10.1007/s10853-012-6260-2).
- [31] N.N. Guo, L. Wang, L.S. Luo, X.Z. Li, R.R. Chen, Y.Q. Su, J.J. Guo, H.Z. Fu, Hot deformation characteristics and dynamic recrystallization of the MoNbHfZrTi refractory high-entropy alloy, *Mater. Sci. Eng. A* 651 (2016) 698–707, doi:[10.1016/j.msea.2015.10.113](https://doi.org/10.1016/j.msea.2015.10.113).
- [32] V. Soni, O.N. Senkov, B. Gwalani, D.B. Miracle, R. Banerjee, Microstructural design for improving ductility of an initially brittle refractory high entropy alloy, *Sci. Rep.* 8 (1) (2018) 8816, doi:[10.1038/s41598-018-27144-3](https://doi.org/10.1038/s41598-018-27144-3).
- [33] N.Y. Yurchenko, N.D. Stepanov, D.G. Shaysultanov, M.A. Tikhonovsky, G.A. Salishchev, Effect of Al content on structure and mechanical properties of the Alx-CrNbTiVZr ($x=0$; 0.25; 0.5; 1) high-entropy alloys, *Mater. Charact.* 121 (2016) 125–134, doi:[10.1016/j.matchar.2016.09.039](https://doi.org/10.1016/j.matchar.2016.09.039).
- [34] N.Y. Yurchenko, N.D. Stepanov, S.V. Zherebtsov, M.A. Tikhonovsky, G.A. Salishchev, Structure and mechanical properties of B2 ordered refractory AlNbTiVZr ($x=0$ –1.5) high-entropy alloys, *Mater. Sci. Eng. A* 704 (2017) 82–90, doi:[10.1016/j.msea.2017.08.019](https://doi.org/10.1016/j.msea.2017.08.019).
- [35] B. Schuh, B. Völker, J. Todt, N. Schell, L. Perrière, J. Li, J.P. Couziné, A. Hohenwarter, Thermodynamic instability of a nanocrystalline, single-phase TiZrNbHfTa alloy and its impact on the mechanical properties, *Acta Mater.* 142 (2018) 201–212, doi:[10.1016/j.actamat.2017.09.035](https://doi.org/10.1016/j.actamat.2017.09.035).
- [36] S. Wang, M. Wu, D. Shu, G. Zhu, D. Wang, B. Sun, Mechanical instability and tensile properties of TiZrHfNbTa high entropy alloy at cryogenic temperatures, *Acta Mater.* 201 (2020) 517–527, doi:[10.1016/j.actamat.2020.10.044](https://doi.org/10.1016/j.actamat.2020.10.044).
- [37] J.P. Couziné, L. Liliensten, Y. Champion, G. Dirras, L. Perrière, I. Guillot, On the room temperature deformation mechanisms of a TiZrHfNbTa refractory high-entropy alloy, *Mater. Sci. Eng. A* 645 (2015) 255–263, doi:[10.1016/j.msea.2015.08.024](https://doi.org/10.1016/j.msea.2015.08.024).
- [38] H.Y. Yasuda, Y. Yamada, K. Cho, T. Nagase, Deformation behavior of HfNbTaTiZr high entropy alloy single crystals and polycrystals, *Mater. Sci. Eng. A* 809 (2021) 140983, doi:[10.1016/j.msea.2021.140983](https://doi.org/10.1016/j.msea.2021.140983).
- [39] Z. Lin, E.J. Lavernia, F.A. Mohamed, High-temperature deformation in a Ta-W alloy, *Acta Mater.* 47 (4) (1999) 1181–1194, doi:[10.1016/S1359-6454\(98\)00434-0](https://doi.org/10.1016/S1359-6454(98)00434-0).
- [40] P.M. Kellner, R. Völkl, U. Glatzel, Influence of ingot and powder metallurgy production route on the tensile creep behavior of Mo-9Si-8B alloys with additions of Al and Ge, *Adv. Eng. Mater.* 20 (1) (2018) 1700751, doi:[10.1002/adem.201700751](https://doi.org/10.1002/adem.201700751).
- [41] J. Wadsworth, S.E. Dougherty, T.G. Nieh, P.A. Kramer, Evidence for dislocation glide controlled creep in niobium-base alloys, *Scr. Metall. Mater.* 27 (1) (1992) 71–76 http://inis.iaea.org/search/search.aspx?orig_q=RN:24014172.
- [42] T. Cao, J. Shang, J. Zhao, C. Cheng, R. Wang, H. Wang, The influence of Al elements on the structure and the creep behavior of AlxCrFeNi high entropy alloys, *Mater. Lett.* 164 (2016) 344–347, doi:[10.1016/j.matlet.2015.11.016](https://doi.org/10.1016/j.matlet.2015.11.016).
- [43] Y.B. Kang, S.H. Shim, K.H. Lee, S.I. Hong, Dislocation creep behavior of CoCr-FeMnNi high entropy alloy at intermediate temperatures, *Mater. Res. Lett.* 6 (12) (2018) 689–695, doi:[10.1080/21663831.2018.1543731](https://doi.org/10.1080/21663831.2018.1543731).
- [44] W.J. Kim, H.T. Jeong, H.K. Park, K. Park, T.W. Na, E. Choi, The effect of Al to high-temperature deformation mechanisms and processing maps of Al0.5CoCrFeMnNi high entropy alloy, *J. Alloys Compd.* 802 (2019) 152–165, doi:[10.1016/j.jallcom.2019.06.099](https://doi.org/10.1016/j.jallcom.2019.06.099).
- [45] Y.-K. Kim, S. Yang, K.-A. Lee, Compressive creep behavior of selective laser melted CoCrFeMnNi high-entropy alloy strengthened by in-situ formation of nano-oxides, *Addit. Manuf.* 36 (2020) 101543, doi:[10.1016/j.addma.2020.101543](https://doi.org/10.1016/j.addma.2020.101543).
- [46] P. Kral, W. Blum, J. Dvorak, N. Yurchenko, N. Stepanov, S. Zherebtsov, L. Kunicka, M. Kvapilova, V. Sklenicka, Creep behavior of an AlTiVNbZr0.25 high entropy alloy at 1073 K, *Mater. Sci. Eng. A* 783 (2020) 139291, doi:[10.1016/j.msea.2020.139291](https://doi.org/10.1016/j.msea.2020.139291).
- [47] M. Zhang, E.P. George, J.C. Gibeling, Tensile creep properties of a CrMnFeCoNi high-entropy alloy, *Scr. Mater.* 194 (2021) 113633, doi:[10.1016/j.scriptamat.2020.113633](https://doi.org/10.1016/j.scriptamat.2020.113633).
- [48] M. Zhang, E.P. George, J.C. Gibeling, Elevated-temperature deformation mechanisms in a CrMnFeCoNi high-entropy alloy, *Acta Mater.* 218 (2021) 117181, doi:[10.1016/j.actamat.2021.117181](https://doi.org/10.1016/j.actamat.2021.117181).
- [49] C. Gadelmeier, S. Haas, T. Lienig, A. Manzoni, M. Feuerbacher, U. Glatzel, Temperature dependent solid solution strengthening in the high entropy alloy CrMnFeCoNi in single crystalline state, *Metals (Basel)* 10 (11) (2020), doi:[10.3390/met10111412](https://doi.org/10.3390/met10111412).
- [50] P. Gong, J. Jin, L. Deng, S. Wang, J. Gu, K. Yao, X. Wang, Room temperature nanoindentation creep behavior of TiZrHfBeCu(Ni) high entropy bulk metallic glasses, *Mater. Sci. Eng. A* 688 (2017) 174–179, doi:[10.1016/j.msea.2017.01.094](https://doi.org/10.1016/j.msea.2017.01.094).
- [51] O.N. Senkov, S. Gorsse, D.B. Miracle, High temperature strength of refractory complex concentrated alloys, *Acta Mater.* 175 (2019) 394–405, doi:[10.1016/j.actamat.2019.06.032](https://doi.org/10.1016/j.actamat.2019.06.032).
- [52] V. Soni, B. Gwalani, T. Alam, S. Dasari, Y. Zheng, O.N. Senkov, D. Miracle, R. Banerjee, Phase inversion in a two-phase, BCC+B2, refractory high entropy alloy, *Acta Mater.* 185 (2020) 89–97, doi:[10.1016/j.actamat.2019.12.004](https://doi.org/10.1016/j.actamat.2019.12.004).
- [53] H.A. Dabkowska, A.B. Dabkowski, R. Hermann, J. Priede, G. Gerbeth, Floating zone growth of oxides and metallic alloys, in: *Handbook of Crystal Growth*, 2nd Edition, Elsevier, Boston, 2015, pp. 281–329, doi:[10.1016/B978-0-444-63303-3.00008-0](https://doi.org/10.1016/B978-0-444-63303-3.00008-0).
- [54] R.R. Eleti, T. Bhattacharjee, A. Shibata, N. Tsuji, Unique deformation behavior and microstructure evolution in high temperature processing of HfNbTaTiZr refractory high entropy alloy, *Acta Mater.* 171 (2019) 132–145, doi:[10.1016/j.actamat.2019.04.018](https://doi.org/10.1016/j.actamat.2019.04.018).
- [55] R.R. Eleti, A.H. Chokshi, A. Shibata, N. Tsuji, Unique high-temperature deformation dominated by grain boundary sliding in heterogeneous necklace structure formed by dynamic recrystallization in HfNbTaTiZr BCC refractory high entropy alloy, *Acta Mater.* 183 (2020) 64–77, doi:[10.1016/j.actamat.2019.11.001](https://doi.org/10.1016/j.actamat.2019.11.001).
- [56] R. Völkl, B. Fischer, M. Beschliesser, U. Glatzel, Evaluating strength at ultra-high temperatures—methods and results, *Mater. Sci. Eng. A* 483–484 (2008) 587–589, doi:[10.1016/j.msea.2006.09.171](https://doi.org/10.1016/j.msea.2006.09.171).
- [57] C.A. Schneider, W.S. Rasband, K.W. Eliceiri, NIH Image to ImageJ: 25 years of image analysis, *Nat. Method.* 9 (7) (2012) 671–675, doi:[10.1038/nmeth.2089](https://doi.org/10.1038/nmeth.2089).
- [58] L.N. Brewer, D.P. Field, C.C. Merriman, Mapping and assessing plastic deformation using EBSD, in: *Electron Backscatter Diffraction in Materials Science*, Springer US, Boston, MA, 2009, pp. 251–262, doi:[10.1007/978-0-387-88136-2_18](https://doi.org/10.1007/978-0-387-88136-2_18).
- [59] J. Málek, J. Zýka, F. Lukáč, J. Čížek, L. Kunčická, R. Kocich, Microstructure and mechanical properties of sintered and heat-treated HfNbTaTiZr high entropy alloy, *Metals (Basel)* 9 (12) (2019) 1324, doi:[10.3390/met9121324](https://doi.org/10.3390/met9121324).
- [60] F. Lukac, M. Dudr, R. Musalek, J. Klecka, J. Cimert, J. Cizek, T. Chraska, J. Cizek, O. Melikhova, J. Kuriplach, J. Zýka, J. Malek, Spark plasma sintering of gas atomized high-entropy alloy HfNbTaTiZr, *J. Mater. Res.* 33 (19) (2018) 3247–3257, doi:[10.1557/jmr.2018.320](https://doi.org/10.1557/jmr.2018.320).
- [61] L. Mataveli Suave, J. Cormier, P. Villechaise, D. Bertheau, G. Benoit, G. Cailletaud, L. Marcin, Anisotropy in creep properties of DS200 + Hf alloy, *Mater. High Temp.* 33 (4–5) (2016) 361–371, doi:[10.1080/09603409.2016.1159836](https://doi.org/10.1080/09603409.2016.1159836).
- [62] O.D. Sherby, P.M. Burke, Mechanical behavior of crystalline solids at elevated temperature, *Prog. Mater. Sci.* 13 (1968) 323–390, doi:[10.1016/0079-6425\(68\)90024-8](https://doi.org/10.1016/0079-6425(68)90024-8).
- [63] M.T. Perez-Prado, M.E. Kissner, Chapter 5 - the 3-power-law viscous glide creep, in: *Fundamentals of Creep in Metals and Alloys*, 3rd Edition, Butterworth-Heinemann, Boston, 2015, pp. 129–138, doi:[10.1016/B978-0-08-099427-7.00005-0](https://doi.org/10.1016/B978-0-08-099427-7.00005-0).
- [64] F.A. Mohamed, T.G. Langdon, The transition from dislocation climb to viscous glide in creep of solid solution alloys, *Acta Metall.* 22 (6) (1974) 779–788, doi:[10.1016/0001-6160\(74\)90088-1](https://doi.org/10.1016/0001-6160(74)90088-1).
- [65] G.A. Henshall, M.E. Kissner, H.J. McQueen, Dynamic restoration mechanisms in Al-5.8 At. Pct Mg deformed to large strains in the solute drag regime, *Metall. Trans. A* 23 (3) (1992) 881–889, doi:[10.1007/BF02675565](https://doi.org/10.1007/BF02675565).
- [66] H.T. Jeong, H.K. Park, H.S. Kang, W.J. Kim, Operation of solute-drag creep in an AlCoCrFeMnNi high-entropy alloy and enhanced hot workability, *J. Alloys Compd.* 824 (2020) 153829, doi:[10.1016/j.jallcom.2020.153829](https://doi.org/10.1016/j.jallcom.2020.153829).
- [67] R.R. Vandervoort, The creep behavior of W-5 re, *Metall. Mater. Trans. B* 1 (4) (1970) 857–864, doi:[10.1007/BF02811765](https://doi.org/10.1007/BF02811765).
- [68] J. Wadsworth, C.A. Roberts, E.H. Rennhack, Creep behaviour of hot isostatically pressed niobium alloy powder compacts, *J. Mater. Sci.* 17 (9) (1982) 2539–2546, doi:[10.1007/BF00543885](https://doi.org/10.1007/BF00543885).
- [69] R.H. Tritan, W.D. Klopp, Long-time creep behavior of the niobium alloy C-103, *NASA Techn. Paper* 1727 (1980) <https://ntrs.nasa.gov/search.jsp?R=19800025047>.
- [70] K. Kashihara, F. Inoko, Effect of piled-up dislocations on strain induced boundary migration (SIBM) in deformed aluminum bicrystals with originally $\Sigma 3$ twin boundary, *Acta Mater.* 49 (15) (2001) 3051–3061, doi:[10.1016/S1359-6454\(01\)00211-7](https://doi.org/10.1016/S1359-6454(01)00211-7).
- [71] A.H. Cottrell, M.A. Jaswon, Distribution of solute atoms round a slow dislocation, *Proc. R. Soc. Lond. A* 199 (1056) (1949) 104–114, doi:[10.1098/rspa.1949.0128](https://doi.org/10.1098/rspa.1949.0128).
- [72] C. Herring, Diffusional viscosity of a polycrystalline solid, *J. Appl. Phys.* 21 (5) (1950) 437–445, doi:[10.1063/1.1699681](https://doi.org/10.1063/1.1699681).
- [73] B.A. Chin, G.M. Pound, W.D. Nix, The role of diffusion in determining the controlling creep mechanisms in Al-Zn solid-solutions: part I, *Metall. Trans. A* 8 (10) (1977) 1517–1522, doi:[10.1007/BF02644854](https://doi.org/10.1007/BF02644854).

- [74] R. Fuentes-Samaniego, W.D. Nix, Appropriate diffusion coefficients for describing creep processes in solid solution alloys, *Scr. Metall.* 15 (1) (1981) 15–20, doi:[10.1016/0036-9748\(81\)90129-0](https://doi.org/10.1016/0036-9748(81)90129-0).
- [75] B. Burton, The influence of solute drag on dislocation creep, *Philos. Mag. A* 46 (4) (1982) 607–616, doi:[10.1080/01418618208236916](https://doi.org/10.1080/01418618208236916).
- [76] M.S. Soliman, I. El-Galali, Appropriate diffusion coefficients for dislocation creep in solid-solution alloys, *J. Mater. Sci. Lett.* 7 (10) (1988) 1027–1030, doi:[10.1007/BF00720814](https://doi.org/10.1007/BF00720814).
- [77] A. Heckl, S. Neumeier, M. Göken, R.F. Singer, The effect of Re and Ru on γ/γ' microstructure, γ -solid solution strengthening and creep strength in nickel-base superalloys, *Mater. Sci. Eng. A* 528 (9) (2011) 3435–3444, doi:[10.1016/j.msea.2011.01.023](https://doi.org/10.1016/j.msea.2011.01.023).
- [78] R.C. Reed, T. Tao, N. Warnken, Alloys-By-Design: application to nickel-based single crystal superalloys, *Acta Mater.* 57 (19) (2009) 5898–5913, doi:[10.1016/j.actamat.2009.08.018](https://doi.org/10.1016/j.actamat.2009.08.018).
- [79] J. Zhang, C. Gadelmeier, S. Sen, R. Wang, X. Zhang, Y. Zhong, U. Glatzel, B. Grabowski, G. Wilde, S.V. Divinski, Zr diffusion in BCC refractory high entropy alloys: a case of 'non-sluggish' diffusion behavior, *Acta Mater.* 233 (2022) 117970, doi:[10.1016/j.actamat.2022.117970](https://doi.org/10.1016/j.actamat.2022.117970).
- [80] S. Guo, C.T. Liu, Phase stability in high entropy alloys: formation of solid-solution phase or amorphous phase, *Prog. Nat. Sci.: Mater. Int.* 21 (6) (2011) 433–446, doi:[10.1016/S1002-0071\(12\)60080-X](https://doi.org/10.1016/S1002-0071(12)60080-X).
- [81] O.N. Senkov, D.B. Miracle, Effect of the atomic size distribution on glass forming ability of amorphous metallic alloys, *Mater. Res. Bull.* 36 (12) (2001) 2183–2198, doi:[10.1016/S0025-5408\(01\)00715-2](https://doi.org/10.1016/S0025-5408(01)00715-2).
- [82] G. Laplanche, P. Gadaud, L. Perrière, I. Guillot, J.P. Couzinié, Temperature dependence of elastic moduli in a refractory HfNbTaTiZr high-entropy alloy, *J. Alloys Compd.* 799 (2019) 538–545, doi:[10.1016/j.jallcom.2019.05.322](https://doi.org/10.1016/j.jallcom.2019.05.322).
- [83] M.E. Glicksman, *Diffusion in Solids : Field theory, Solid-State principles, and Applications*, Wiley, New York, 2000.
- [84] R.C. Reed, *The Superalloys : Fundamentals and Applications*, Cambridge University Press, Cambridge, 2006.
- [85] A. Janotti, M. Krčmar, C.L. Fu, R.C. Reed, Solute diffusion in metals: larger atoms can move faster, *Phys. Rev. Lett.* 92 (8) (2004) 085901, doi:[10.1103/PhysRevLett.92.085901](https://doi.org/10.1103/PhysRevLett.92.085901).